*Journal of the Meteorological Society of Japan*, **99**(5), 1231−1252, 2021. doi:10.2151/jmsj.2021-060 
Special Edition on Global Precipitation Measurement (GPM): 5th Anniversary

# Refinement of Surface Precipitation Estimates for the Dual-frequency Precipitation Radar on the GPM Core Observatory Using Near-Nadir Measurements

**Masafumi HIROSE**

*Faculty of Science and Technology, Meijo University, Nagoya, Japan*

**Shoichi SHIGE**

*Graduate School of Science, Kyoto University, Kyoto, Japan*

**Takuji KUBOTA**

*Earth Observation Research Center, Japan Aerospace Exploration Agency, Tsukuba, Japan*

**Fumie A. FURUZAWA, Haruya MINDA, and Hirohiko MASUNAGA**

*Institute for Space-Earth Environmental Research, Nagoya University, Nagoya, Japan*

*(Manuscript received 1 October 2020, in final form 21 May 2021)*

## Abstract

Precipitation statistics from Global Precipitation Measurement Core Observatory Dual-frequency Precipitation Radar (GPM DPR) are underestimated due to systematic bias depending on the scanning angle. Over five years of GPM DPR KuPR Version 06A data, the precipitation anomaly is −7 % and −2 % over land and ocean, respectively. This study improves the estimation of low-level precipitation-rate profiles and the detection of shallow storms (with top heights of ≤ 2.5 km), using reference datasets of near-nadir measurements.

First, the low-level precipitation profile (LPP) is updated using an a priori near-nadir database generated from structural-characteristics related variables of the precipitation and environmental parameters. The LPP correction increases precipitation over areas where downward-increasing precipitation profiles are dominant below 2 km, such as at high elevations and at middle and high latitudes. Globally, the LPP correction increases precipitation by 5 %. Second, the effect on precipitation data of missing shallow storms is estimated using the angle-bin difference in the detectability of storms with a top height of ≤ 2.5 km. The effect of the shallow-precipitation deficiency (SPD) is comparable in magnitude to that of the LPP correction. A priori lookup tables for the SPD correction, constrained by the clutter-free bottom level and spatially averaged shallow-precipitation fractions, are constructed so that the correction applies to gridded statistics at 0.1° and three-month scales. The SPD correction enhances precipitation by 50 % over specific low-rainfall oceans in the sub-tropics and at high latitudes, where shallow precipitation dominates. Based on these two corrections, precipitation increases by 8 % and 11 % over land and ocean, respectively. At latitudes between 60°N and 60°S, the difference in KuPR compared with satellite-gauge blended products is reduced from −17 % to −9 %, whereas with gauge-based products is reduced from −19 % to −15 % over land.

Corresponding author: Masafumi Hirose, Faculty of Science and Technology, Meijo University, 1-501, Shiogamaguchi, Tempaku, Nagoya, Aichi 468-8502, Japan
E-mail: mhirose@meijo-u.ac.jp
J-stage Advance Published Date: 8 June 2021

**Keywords** spaceborne precipitation radar; retrieval error; low-level precipitation profile; shallow storm; surface-clutter mask; incidence-angle dependence

**Citation** Hirose, M., S. Shige, T. Kubota, F. A. Furuzawa, H. Minda, and H. Masunaga, 2021: Refinement of surface precipitation estimates for the Dual-frequency Precipitation Radar on the GPM Core Observatory using near-nadir measurements. *J. Meteor. Soc. Japan*, **99**, 1231–1252, doi:10.2151/jmsj.2021-060.

## 1. Introduction

The geographical distribution of precipitation can be delineated using high-volume data obtained from spaceborne precipitation radars: the Tropical Rainfall Measuring Mission Precipitation Radar (TRMM PR) (Kummerow et al. 1998; Kozu et al. 2001) and the Global Precipitation Measurement Core Observatory Dual-frequency Precipitation Radar (GPM DPR) (Kojima et al. 2012; Hou et al. 2014; Skofronick-Jackson et al. 2017; Iguchi 2020; Nakamura 2021). Compared to the ground observations, restricted by the locations of the measuring stations, satellite products are superior in representing spatial information (Beck et al. 2019; Sun et al. 2018). Spaceborne radars onboard non-sun-synchronous satellites detect echoes regardless of surface type and local time zone and can investigate the striking dependence of precipitation on environmental features (e.g., Hamada et al. 2015; Liu and Zipser 2015; Hirose et al. 2017). However, the current observational precipitation datasets need refinement to understand the complete magnitude of the global water and energy cycles (Adler et al. 2017a; Behrangi et al. 2014; Stephens et al. 2012). Advances in fine-scale precipitation mapping have increased the need to mitigate regional retrieval errors. In addition to problems of insufficient sensitivity and sampling uncertainty, attention needs to be paid to attenuation corrections, varying drop-size distributions, non-uniform beam-filling effects, and bright band detection (Iguchi et al. 2009; Seto et al. 2013, 2021; Kubota et al. 2014, 2020a; Awaka et al. 2016; Meneghini et al. 2015, 2021). Improvements in algorithms and statistical evaluations have been ongoing since the late 20th century. The underestimation of precipitation in spaceborne radar data has been highlighted in several studies (e.g., Kirstetter et al. 2013; Oki et al. 2020; Heymsfield et al. 2020). Despite a diverse array of comparative studies over the last two decades, the algorithmic issues responsible for the known precipitation bias have not been entirely resolved.

Some of the retrieval properties of spaceborne radars depend on the incidence angle. A regional bias in the TRMM PR data is identified using statistical differences between incidence angles (Hirose et al. 2012, hereafter, H12). An accurate observation of the shallow storms becomes difficult at large incidence angles because the interference caused by surface clutter increases toward off-nadir angles. H12 and a short report (Hirose 2011) noted that near-nadir statistics are less affected by removal masks designed to eliminate main-lobe clutter. The authors showed that approximately 5 % of the total precipitation is underestimated in the TRMM PR data because of the deterioration of radar estimates in its off-nadir scans. Also, they show that half of the underestimates are caused by missing shallow storms, whereas the remainder is caused by other reasons, including low-level profile assumptions.

Deep clutter-free bottom (CFB) levels could affect surface precipitation estimates, especially vertically varying precipitation, below the melting layer (e.g., Kobayashi et al. 2018; Liu and Zipser 2013; Terao et al. 2017; Sohn et al. 2015). The GPM DPR products provide two types of precipitation rates at the estimated surface: "precipRateESurface" and "precipRateESurface2". In "precipRateESurface" (standard output), the algorithm estimates a precipitation rate at the surface by assuming that the effective radar reflectivity factor ($Z_e$) at the surface is identical to that at the lowest point free from main-lobe clutter (Seto et al. 2021). This assumption can be challenging because of regional variations in the low-level precipitation profiles (LPP), as identified by H12. Therefore, an extrapolated surface precipitation rate, "precipRateEsurface2", is prepared as an experimental output of the DPR product Version 06A (Iguchi et al. 2018). The correction in "precipRateESurface2" is based on an a priori low-level profile dataset classified by the aloft precipitation rate for each 5° grid cell. However, the development of dynamic correction methods remains a challenge.

Shallow storms interfered with the surface-clutter mask of radar are difficult to detect, especially over mountainous areas/higher latitudes (Aoki and Shige 2021; Barros and Arulraj 2020; Casella et al. 2017). Factors causing underestimation were analyzed in

H12 following statistics from coarse grids or the global mean, because samples of near-nadir statistics must ensure the reliability of the reference data. This sampling issue is mitigated to some extent by accumulating data over a long period. Additionally, high-latitude observations by GPM DPR increased the need to evaluate the effect of missing shallow storms. Therefore, analyses of shallow storm detection based on previous work, involving TRMM PR observations, need to be updated.

This study aims to enhance the consistency of precipitation estimates across angles by reducing the off-nadir underestimation and to improve surface precipitation estimates from spaceborne radars. This paper examines the incidence-angle dependency of spaceborne radars and suggests two correction methods for the incidence-angle dependency of GPM DPR. One is the substitution of the instantaneous estimated precipitation profiles near the surface using an a priori database. The other is a statistical evaluation of the impact of missing shallow storms and the retrieval of the missing data from a lookup table.

The remaining part of this paper is organized as follows: Section 2 describes the incidence-angle dependency of precipitation estimates from spaceborne radars and the two correction methods. The impacts of the corrections are examined in Section 3, while conclusions are given in Section 4.

## 2. Incidence-angle dependency and correction methods

### *2.1 GPM DPR data*

This study uses five years of GPM DPR KuPR Version 06A (hereafter, KuPR) data, from June 2014 to May 2019. In addition, GPM DPR KuPR Version 05A and TRMM PR Versions 7 and 8 products are used for some comparisons. The KuPR sensor is similar to TRMM PR in terms of frequency, horizontal footprint size, and scan width (245 km). However, its sensitivity is superior at approximately 15.5 dBZ against 18 dBZ, and its areas and levels of observation have been extended (Masaki et al. 2020; Iguchi 2020; Kojima et al. 2012; Hou et al. 2014; Hamada and Takayabu 2016). Its horizontal resolution is approximately 5 km. The vertical resolution of both radars is 250 m. Moreover, the sampling intervals of the TRMM PR and KuPR data are 250 m and 125 m, respectively. The number of gridded samples obtained from KuPR is approximately half that obtained from TRMM PR. For instance, TRMM PR and KuPR observe 2.0 and 1.0 samples, respectively, at a 0.1°-grid resolution per day over 20°S–20°N. On average, an overpass observation provides five to six samples for a 0.1° grid cell, i.e., the GPM Core Observatory passes over a certain point in the tropics, once every five to six days. The number of overpasses per day is 0, 1, and 2, accounting for 78 (32), 21 (53), and 1 % (15 %), respectively, for a 0.1° (5°) grid cell over 20°S–20°N. At latitudes between 61.6° and 65.8°, the number of samples obtained from KuPR exceeds that from TRMM PR in the tropics.

Furthermore, the surface precipitation rate ("precipRateESurface") is estimated using the radar reflectivity factor extrapolated down to the main-lobe clutter region. As explained in Section 1, $Z_e$ below the CFB level is set to a constant (Seto et al. 2021), except in the TRMM PR Version 7 product, which includes a downward-decreasing $Z_e$ in the clutter-interfered levels for stratiform precipitation over land, reflecting the evaporation effect assumptions (TRMM Precipitation Radar Team 2011). The precipitation rate ($R$) is calculated for a given $R$–$D_m$ relation once the mass-weighted mean diameter ($D_m$) is retrieved from the radar reflectivity factor (Iguchi et al. 2018; Seto et al. 2013, 2021). Also, the pressure correction is performed on the terminal velocity for the precipitation estimates, which is a possible factor in downward-decreasing precipitation rates for vertically constant $Z_e$. This study focuses on the acceptability of this assumption concerning low-level precipitation profiles (LPPs).

Figure 1 shows the CFB levels. The average levels are approximately 1 km near nadir and 2 km at the edge of the swath. To mitigate contamination by ground clutter, these levels are slightly higher than those for TRMM PR Version 7 over a large part of the land area (Iguchi et al. 2018; Kubota et al. 2016). Note that the topography modulates the spatial pattern. For example, a 0.1° average CFB level over the Himalayas is approximately 1 km higher than that over flat land and oceans, such that the precipitation at altitudes below 2–3 km from the surface is not detected, even at nadir. At latitudes higher than 65°, the average CFB level is high due to the lack of data at low incidence angles.

### *2.2 Angle-dependent retrieval uncertainties*

Precipitation statistics based on TRMM PR and KuPR differ by angles and products, as shown in Fig. 2. Precipitation off nadir is underrepresented when compared to the near-nadir data, except over the ocean at low latitudes. This off-nadir underestimation correlates with the findings of H12 from the TRMM PR data. At high latitudes, estimates of the precipitation decrease, forming a parabola away from nadir. An

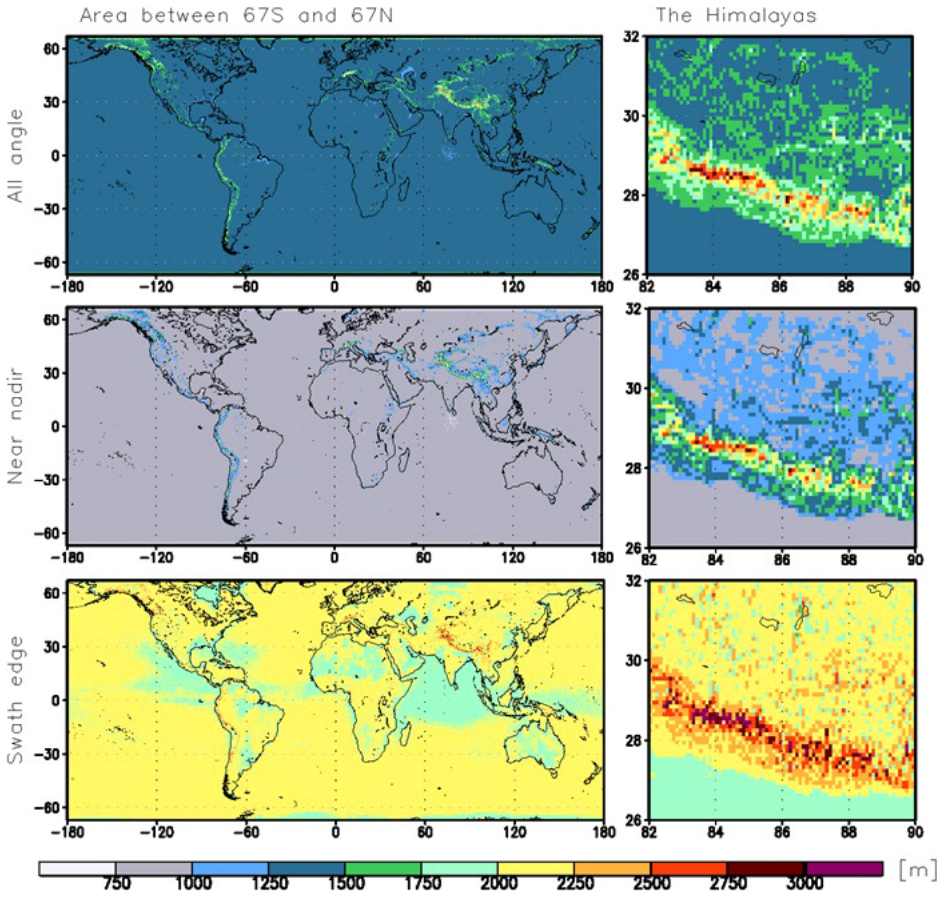


Fig. 1. The level of the lowest range bin free from surface clutter over the entire observational area and the Himalayas based on the five-year GPM Dual-frequency Precipitation Radar (DPR) KuPR Version 06A data using all-angle bins (top), those near nadir (middle), and the swath edges (bottom). The level indicates the height above the surface. The spatial resolution is 0.1°. The near-nadir statistics use data in bins 21–23 and bins 27–29 and the swath-edge statistics are for data in bins 1–2 and bins 48–49.

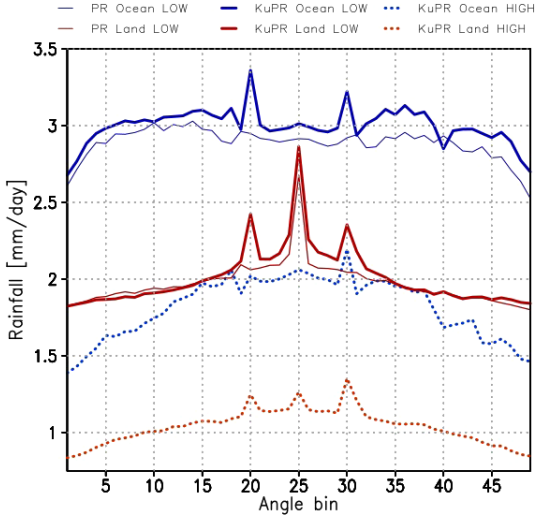


Fig. 2. Surface precipitation over land and ocean for each angle bin. The thick and thin solid lines indicate the averages between 35°S and 35°N (LOW) using the 5-year KuPR Version 06A and 16-year TRMM PR Version 8 data, respectively. The statistics are obtained over the ranges of 66–35°S and 35–66°N (HIGH) using the five-year KuPR Version 06A (dotted lines).

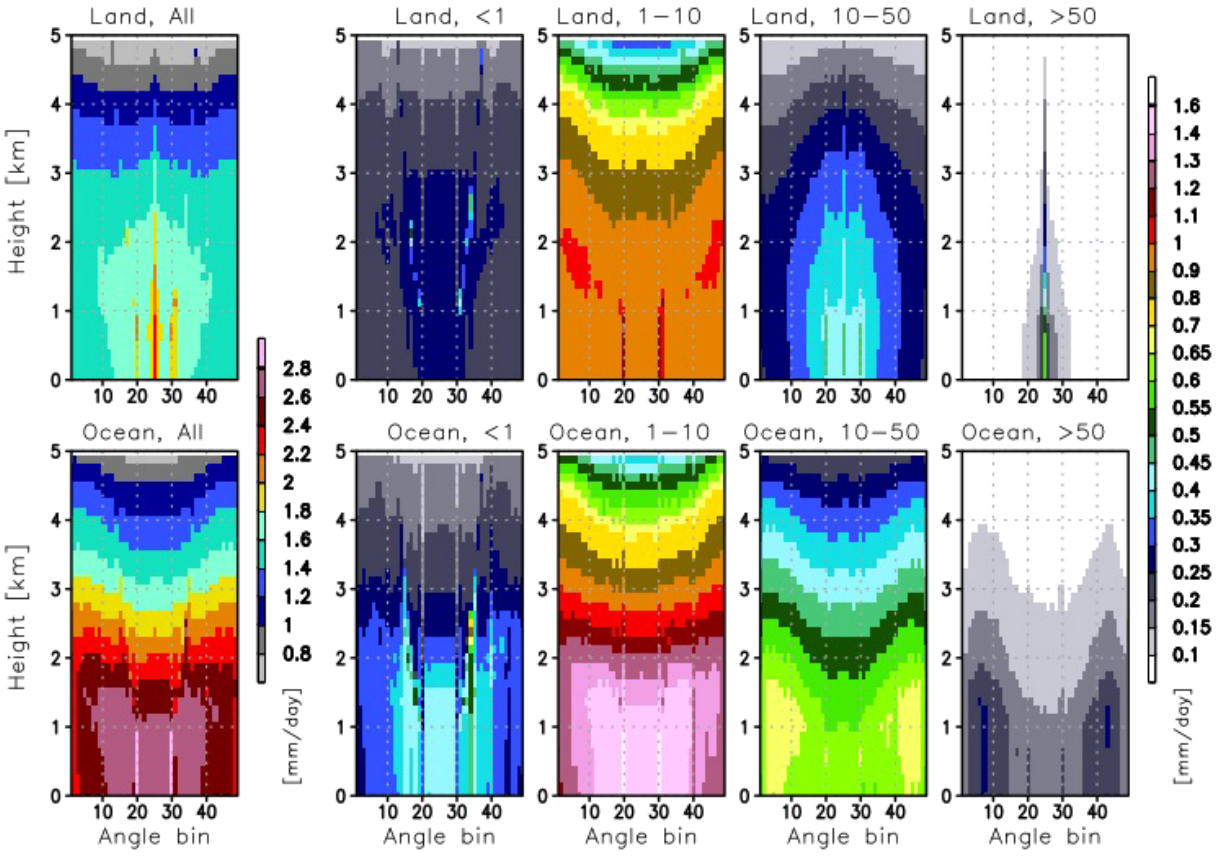


Fig. 3. Vertical distribution of precipitation over the land (upper) and ocean (lower) for each angle bin. From left to right, the different panels show data composites of various surface precipitation rates: all, < 1, 1−10, 10−50, and ≥ 50 mm $h^{-1}$, respectively.

update in the algorithm reduces the side-lobe clutter (Kubota et al. 2016); however, the contamination at bins 20 and 30 remains a positive bias. Precipitation estimates increase by more than 20 % at the nadir angle over land. Improvements by each algorithm update have been identified about the reduced incidence-angle difference; however, an angle-dependent bias remains. The TRMM PR Version 7 product reduces side-lobe clutter but leaves an asymmetric bias resulting from the beam-mismatch correction errors (H12, Hirose 2011), different from other DPR algorithm-based products (not shown). Moreover, differences in the near-nadir precipitation between products are seen. This study focuses on mitigating the incidence-angle dependency in the KuPR precipitation data rather than the examination of error factors in different products.

Figure 3 shows that the KuPR precipitation rate of > 50 mm $h^{-1}$ is remarkably high at a nadir over land because of uncertainties in the path-integrated attenuation (PIA) estimates that need to be specified for non-precipitating surface cross-sections in such areas (Meneghini et al. 2015, 2021). Over the land, all precipitation products are underestimated off-nadir, especially at the swath edge, because of the reduced ability of the sensor to detect downward-increasing precipitation rates and its failure to detect shallow storms against the relatively deep CFB. The overall features of the angle-bin difference are consistent with the results of H12, using TRMM PR, except for the clutter impacts from the antenna sidelobes and right–left asymmetric pattern, following the orbit boost in 2001. Over the ocean, weak and moderate precipitation rates smaller than 10 mm $h^{-1}$, are frequently observed in the inner swath. However, the off-nadir underestimates are unclear, except at the swath edge due to the predominant stratiform systems and the cross-track-dependent algorithm in the attenuation-

Table 1. Precipitation and anomalies for the near-nadir statistics between 35°S and 35°N (the parentheses show the statistics for 66–35°S and 35–66°N). The values are from the 16-year TRMM PR data and the 4- and 5-year GPM DPR KuPR Version 05A and 06A data.

| | Ocean | | | | Land | | | |
|---|---|---|---|---|---|---|---|---|
| | PRv.7 | PRv.8 | KuPR05A | KuPR06A | PRv.7 | PRv.8 | KuPR05A | KuPR06A |
| Precipitation [mm $d^{-1}$] | 2.6 | 2.9 | 3.1 (−1.9) | 3.0 ( 1.8) | 2.2 | 2.0 | 2.1 ( 1.1) | 2.0 ( 1.0) |
| Anomaly [%] | −4.0 | −0.2 | 1.7 (−7.9) | 0.7 (−8.8) | −4.7 | −5.1 | −11.8 (11.6) | −6.4 (−8.8) |

correction procedure. Overestimates of strong precipitation rates in the outer swath, over the ocean, could be attributed to the attenuation-correction effect based on the differential surface cross-section estimated from the along- and cross-track reference data, and the fitting function, referred to as the hybrid surface reference technique (Meneghini et al. 2004, 2015; Seto and Iguchi 2007), similar to the results in H12 from TRMM PR.

The reference in this study is the near-nadir statistics. In the cross-track direction, 1st–49th angle-bin data are observed with an interval of 0.71° from the nadir (bin 25). H12 set their reference data to bins 23–24 out of 49 over land and bins 23–25 over the ocean considering the lowest CFB, insignificant sidelobe contamination, uncertainty in the heavy precipitation over land, and non-symmetric patterns due to the beam-mismatch effect. In this study, given the update to the algorithm and consistency of the statistics, we use the reference data from the precipitation data in bins 21–23 and bins 27–29. Additionally, the nadir precipitation rate of $< 50$ mm $h^{-1}$ over the land is used to generate the low-level profile database.

Compared to the near-nadir statistics, the underestimation bias in the surface KuPR precipitation is 7 % and 2 % over the land and ocean (66°S–66°N), respectively. At low latitudes, significant underestimates are found over land; however, the oceanic precipitation is slightly higher than the reference (Table 1). Regarding the middle-to-high latitudes, precipitation is 9 % lower than the near-nadir statistics over land and ocean. The differences are reduced at higher levels. Highlighting the vertical cross-section of average precipitation between angles, Fig. 3 shows that the remarkable incidence-angle difference appears at lower levels. Several features such as the off-nadir increase in intense precipitation over the ocean and their peak at a nadir over the land are observed. However, the largest impact on the total amount of precipitation is by moderate precipitation of less than 10 mm $h^{-1}$, and the total incidence-angle dependency results in underestimation.

### *2.3 Low-level precipitation profile (LPP) database*

As noted in Section 2.1, in the current GPM DPR algorithm, precipitation-rate profiles in the clutter region are estimated by assuming a constant $Z_e$ and modified drop-size distribution parameters; however, various low-level profiles have been observed. This study prepares near-surface profiles, below the CFB level, based on a LPP database generated from near-nadir statistics. The constraints of the LPP database are the surface type (2 bins), precipitation type (2 bins), 0°C levels (8 bins), storm top height (STH: 6 bins), and vertical gradients of the precipitation rate (VGP: 7 bins) at 2–2.5 km or 3–3.5 km above the surface (Fig. 4). The STH is the highest of three consecutive meaningful precipitation echoes. We define the VGP as the gradient of the regression line using precipitation rates in five range bins between 2 km and 2.5 km (in most cases). The present LPP database contains 1,344 profiles corresponding to the abovementioned variables. In addition, another database for CFB levels at 2–3 km and their average profiles are prepared. For a shallow storm where VGP at 2–2.5 km is not obtained, the reference profile (averaged without VGP) is used as a substitute. This substitution is applied to profiles with a CFB level of $< 2$ km. In mountainous regions where CFB $\geq 2$ km, another LPP database measuring values below 3 km with VGP at 3–3.5 km is applied. The near-nadir profile information in the clutter region, approximately below 1 km, is derived based on the standard algorithm. Therefore, this correction enables the mitigation of different LPPs between angles.

Figure 5 shows a simplified version of LPP averaged separately for stratiform and convective precipitation over land and ocean. These profiles are averaged for different conditions: deep and non-deep storms (threshold STH, 6 km), downward increasing and constant or downward-decreasing profiles (threshold VGP at 2–2.5 km, −0.5 mm $h^{-1}$ $km^{-1}$), and warm and cold environments (threshold 0°C level, 2 km). The original LPP database is further subdivided using these parameters. Figure 5 shows that LPPs are characterized

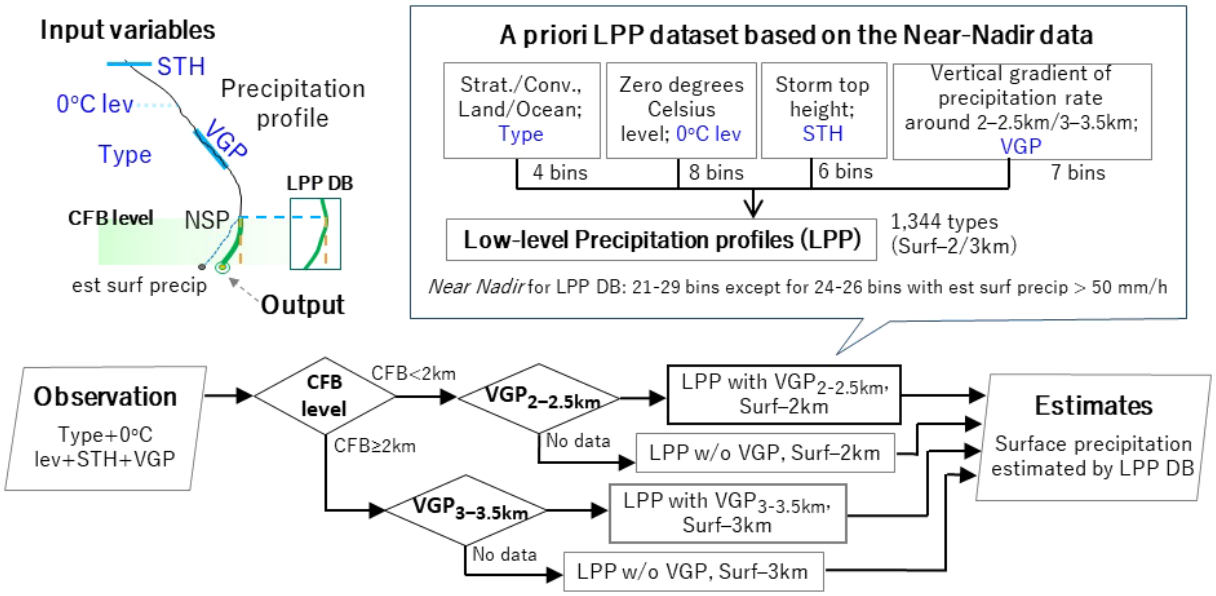


Fig. 4. Flowchart of the low-level precipitation profile correction.

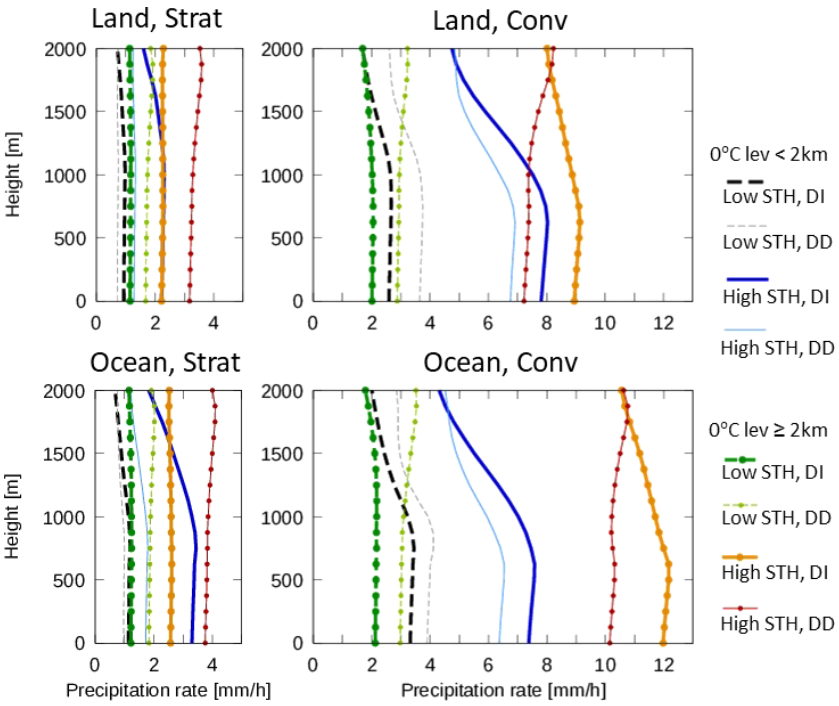


Fig. 5. Examples of simplified LPP average for stratiform (left) and convective (right) precipitation over land (upper) and ocean (lower). Solid-dashed lines indicate LPP when the storm top height is ≥ 6 km (high STH) and < 6 km (low STH), respectively. Thick lines correspond to the downward-increasing (DI) profiles with VGP < −0.5 mm $h^{-1}$ $km^{-1}$, whereas thin lines correspond to the constant or downward-decreasing (DD) profiles with VGP ≥ −0.5 mm $h^{-1}$ $km^{-1}$. Lines with marks represent LPP average for 0°C levels of ≥ 2 km, whereas those without marks represent LPP average for 0°C levels of < 2 km.

by significant downward-increasing patterns and slight decreasing patterns. For downward-increasing profiles with storm top heights of ≥ 6 km and 0°C levels of < 2 km, as shown by the thick blue solid lines, the precipitation rates at the surface are approximately 1.5 times greater than those at 2 km. Significant differences in the precipitation rates, below 2 km, are observed for deep convective storms, as indicated by the solid lines. In convective precipitation, LPPs for tropical deep storms (solid orange and red lines) have similar precipitation rates at 2 km but differ considerably near the surface, implying the significant impact of VGP aloft. The precipitation rate does not change significantly for stratiform precipitation, except for the abovementioned deep storms with downward-increasing VGP at high latitudes. Consistent with earlier studies (Hirose and Nakamura 2004; Liu and Zipser 2013; Kobayashi et al. 2018; Porcacchia et al. 2019), precipitation rates are possibly increasing toward the surface in low-temperature regions. The low-level peaks below 1 km often appear with even moderately downward-decreasing VGP. Thus, the profile of near-surface precipitation rate is not fully determined as an extension of the upper part of the profile. The LPP database includes profiles with bimodal structures at high latitudes.

The height-smearing effect is not considered in the LPP correction. Therefore, vertical properties, such as VGP, become slightly blurred at its off-nadir. For example, VGP at the scan edge (17°) could be approximately 4 % smaller than that at the nadir. In this study, it is expected that the height-smearing effect on the LPP correction will be small, since the absolute value of the vertical information is roughly divided. For example, VGP is classified into seven categories with the thresholds of −5, −2, −0.5, 0.5, 2, and 5 mm $h^{-1}$ $km^{-1}$. Thus, this LPP correction incorporates patterns of various low-level profiles, which could be conservative for extreme cases with few samples.

Note that the LPP correction does not ensure consistency with attenuation estimates. The PIA estimate of the single-frequency algorithm is operationally based on the Hitschfeld–Bordan (HB) method and surface reference technique (SRT) (Iguchi et al. 2018; Meneghini et al. 2021). Although the forward procedure based on the former method works for lighter precipitation, it increases the retrieval uncertainties in cumulative attenuation near the surface. The PIA estimate given by SRT is based on the difference in the surface echoes with and without precipitation. The backward-correction method with a constraint on the total attenuation estimates is stable for intense precipitation. The LPP correction below the CFB level could affect PIA estimates through the forward approach and the adjustment factor of the modified HB–SRT method, particularly for heavy precipitation. An iterative approach using profile databases of measured radar reflectivity ($Z_m$) might represent the coherent-spatial structure of precipitation; however, in this study, a posterior scheme based on the LPP database is applied for simplicity. Moreover, the issue regarding attenuation correction is addressed in Section 3.3a.

### *2.4 Shallow-precipitation deficiency (SPD)*

H12 investigated the idea that the underestimation of off-nadir precipitation from shallow storms is caused by the smaller number of observed shallow systems and that the impact of this effect is high over the ocean. Significant angle-bin differences in the histogram of STH appear approximately below 2 km. This study applies the same approach to estimate the impact of missing shallow storms on the KuPR data. The incidence-angle discrepancy of the surface precipitation from the difference in the number of missing shallow storms is retrieved using the near-nadir (nn) precipitation intensity at the surface ($\overline{R_s}$), conditioned on the STH and stratiform/convective (sc) types, and the categorized storms detected at each angle, as shown in Eq. (1), where $N$ is the number of storms for each angle, STH, and precipitation type. The near-nadir $N$ is an average of $N$ at the 21st–23rd and 27th–29th angle bins. The equation shows the fraction of missing precipitation resulting from the angle-bin differences in the number of STH ≤ 2.5 km and corresponding surface precipitation intensity at each grid to the near-nadir total precipitation. In this study, the effect estimated from fewer samples because of the deteriorating CFB levels is referred to as the SPD. In H12, a threshold of 3 km above the surface was set as the STH of shallow storms, allowing some amount of sampling at all-angle bins, consistent with the natural statistics of shallow storms along with trade wind

$$\mathrm{SPD} = \frac{\sum_{i=1}^{49}\sum_{h=\mathrm{surf}}^{2.5\mathrm{km}}\sum_{k=\mathrm{sc}}[N(i,h,k)-N(\mathrm{nn},h,k)]\overline{R_s}(\mathrm{nn},h,k)}{49\sum_{h=\mathrm{surf}}^{\mathrm{top}}\sum_{k=\mathrm{sc}}N(\mathrm{nn},h,k)\overline{R_s}(\mathrm{nn},h,k)}, \quad (1)$$

inversion. In this study, shallow storms are defined as precipitation echoes with an STH of ≤ 2.5 km to mitigate the height-smearing effect resulting from matching per-level samples in each 125-m range bin between angles. The previous study used the data in the first half scan in their bias estimation to isolate the beam-mismatch effect (for details, see Section 2b of H12). This study uses all-angle data observed by KuPR, considering the symmetric pattern shown in Fig. 2. It is easy to see that SPD has a negative value. In this study, the SPD effect indicates the effect of the complement processing of SPD as a positive value, as shown in Eq. (2):

$$\text{SPD effect} = -\frac{100\text{SPD}}{1+\text{SPD}}. \tag{2}$$

For example, the SPD effect is 25 % for the case where SPD is −0.20.

## 3. Impacts of the LPP and SPD corrections

### *3.1 Correction of LPPs*

LPP corrections are made for every profile using the a priori LPP database. Thus, the vertical precipitation-rate profiles around the CFB level have been corrected to enable smooth connection by the substitution, according to the structural and environmental variables. The positive values in this correction indicate that the low-level profile values are corrected upward compared to the current algorithm assumptions. Figure 6 shows a snapshot of the precipitation and correction effect in the case of Typhoon Megi hitting Taiwan on September 26, 2016. The effect is less significant for moderate precipitation over flat areas in the inner swath where the CFB levels are relatively low. The individual effects often exceeded 10 %. Most of the profiles with downward-increasing precipitation rates near 2–2.5 km show increased precipitation at 1 km. A downward-increasing trend appears in situations, such as orographic precipitation, shallow storms, and mid-latitude disturbances. The LPP correction decreases precipitation lower than 1 mm $h^{-1}$, at the outer edge of the precipitation area, by more than 5 %. The downward-decreasing profiles below CFB are selected from the a priori database, particularly at the edges of stratiform precipitation areas over arid regions, implying a significant evaporation and pressure-correction effect for different precipitation rates. The regional characteristics of low-level profiles of light precipitation with downward-decreasing VGP and the database validity need to be further examined. On average, the decrease in precipitation is negligible, except in low-rainfall areas, as will see in the sequel.

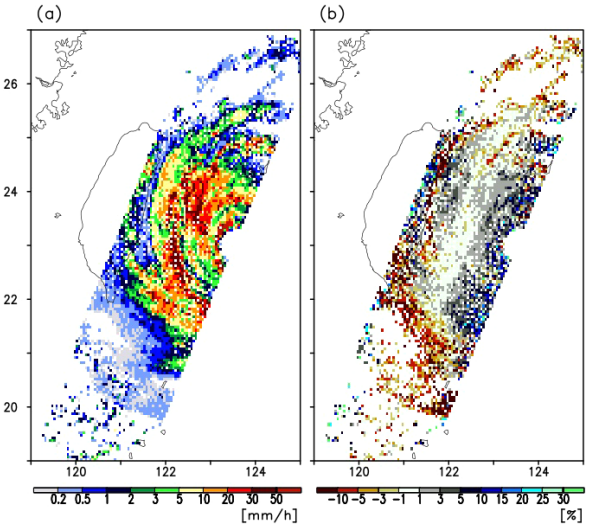


Fig. 6. Snapshot of the (a) rainfall rate and (b) effect of the LPP corrections on the surface precipitation estimates at each 0.05° grid cell for the case of Typhoon Megi hitting Taiwan on September 26, 2016. The positive values in panel (b) indicate that the LPP corrections increase surface rainfall. Pixels where the surface precipitation rate is less than 0.2 mm $h^{-1}$ are blanked out.

On average, the LPP corrections conspicuously increased precipitation in areas where shallow storms are dominant, except for low-rainfall areas, as shown in Fig. 7a. The effect is obvious at the swath edge and over steep terrain, even at nadir (Figs. 7b, c). More than 20 % of the amount of precipitation increased over the northern Atlantic, at latitudes near 60–50°S, along with high mountain ranges, and the northern and southern edges of the orbit. However, the difference is not significant over the Antarctic Ocean, where most storm top heights are lower than 3 km and most low-level profiles are lost because the clutter interference has been removed. Over arid regions, the corrections decreased precipitation by several percentages, indicating a drastic decline in the near-surface precipitation because of evaporation. Over wide areas of the Tibetan Plateau, where shallow storms dominate, the LPP correction increases precipitation by 20 %. One can see a discrete pattern in the north–south-direction tracing satellite orbits with an inclination angle of 65°. This reflects the latitude-dependent regional differences in the CFB levels of individual samples, constrained by the orbit. Note that the precipitation profiles vary with season (not shown). For example, the LPP effect around Japan is insignificant in summer

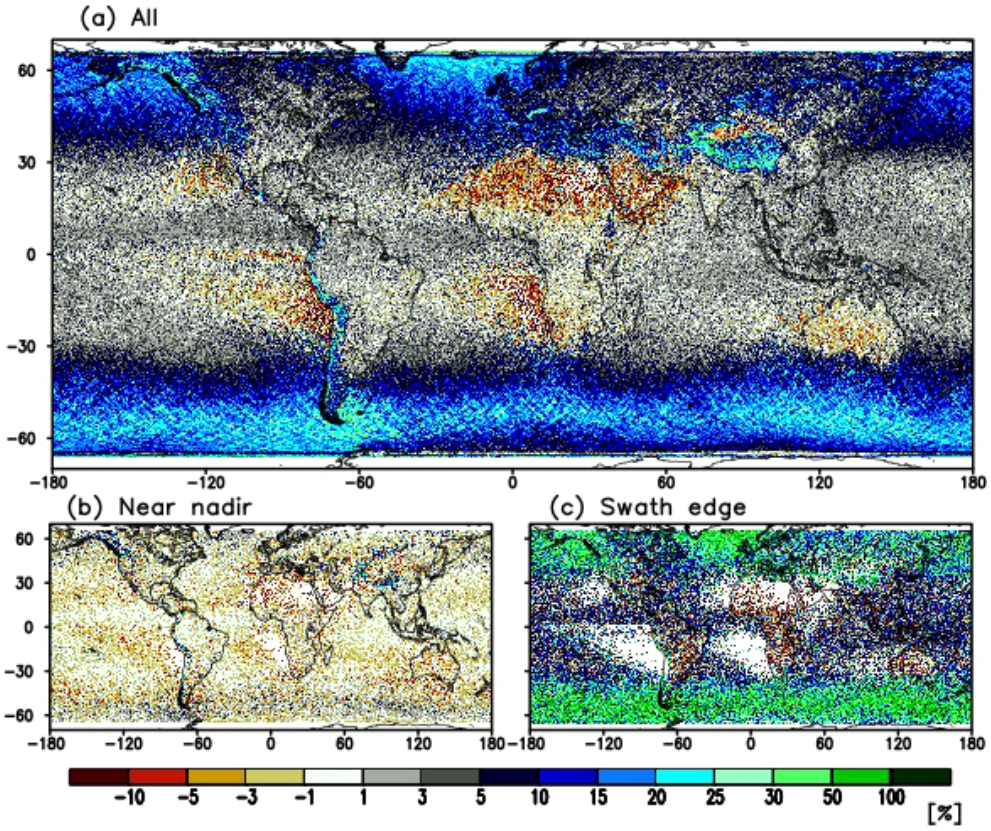


Fig. 7. Effect of the LPP correction (a) between 70°S and 70°N, (b) near nadir, and (c) at the swath edge.

but reaches approximately 20 % in winter. Also, the negative effect or the downward-decreasing trend is significant over the Taklimakan Desert in summer and moderate over land areas during dry winter.

It is worthy to note that VGP or the low-level vertical-gradient information effectively determines the downward increasing and decreasing patterns at low levels. The removal of VGP from the LPP database constraints blurs this effect, particularly in the correction of instantaneous snapshots, as shown in Fig. 6. Over the Sahara (10°W–30°E, 15–30°N) where downward-decreasing profiles prevail, the VGP information on the current LPP correction decreased surface precipitation by approximately 4 % compared with that without this information. The VGP calculated at 3–3.5 km represents the low-level patterns, while the VGP at 2–2.5 km is necessary to perform corrections, particularly for shallow storms at high latitudes. The removal of the VGP parameter at 2–2.5 km from the correction procedure in Fig. 4 deteriorates the positive effect of LPP corrections by approximately 5 % of the total precipitation due to the extratropical cyclones at 60–50°S (not shown).

Our preliminary investigation shows that the spatial pattern of the LPP correction for the TRMM PR Version 8 product is similar to that of the KuPR Version 6 product since their the algorithms are basically the same. However, for the TRMM PR Version 7 product, the positive effect over the land areas is notable (not shown). This may be attributable to the assumption that stratiform precipitation over land decreases in the clutter region by 0.5 dB km$^{-1}$ in the TRMM PR Version 7 algorithm. In addition, the $D_m$ profiles of KuPR may result in differences in the LPP databases of KuPR and TRMM PR Version 7. The source of the inconsistency between these algorithms requires investigation.

Furthermore, the precipitation amount and incidence-angle dependency differ considerably with altitude. This correction modifies the estimated precipitation profiles at levels between approximately 1 km and 2 km and increases the precipitation amount at levels around and below 1 km at off-nadir angles (Figs. 8a, b). Figure 8c shows the impact of the LPP correction

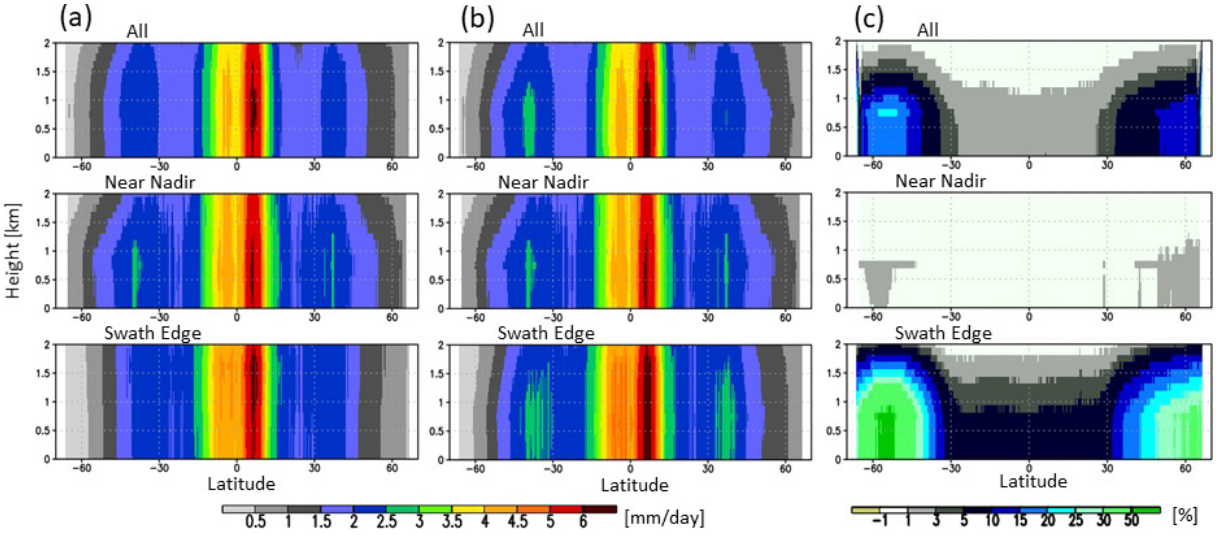


Fig. 8. Latitudinal cross-section of (a) precipitation based on the original data, (b) the LPP-corrected precipitation, and (c) the correction effect based on the KuPR data using all-angle bins (top), those near nadir (middle), and the swath edges (bottom). The ordinate represents the height from the surface up to 2 km.

for each latitude and level above the surface. Even at near-nadir angles, the estimated precipitation below the CFB level slightly increases at high latitudes because some samples contain slightly high CFB levels, as also shown in Fig. 7b. At the swath edge, the near-surface precipitation increases by 5–10 % in the tropics and more than 50 % at 60–50°S because of this correction. The correction has more influences at the northern and southern edges of the observable domains, where no nadir observation is attainable. In addition, the incidence-angle difference before and after the LPP correction is due to the changes made by this correction. The underestimation bias to the near-nadir statistics is noticeable near 1 km before the correction. The LPP correction improves the consistency across the incident angles, while maintaining a negative anomaly. An evaluation of this is summarized in Section 3.3.

### *3.2 Evaluation and estimation of the SPD*

#### *a. Effect of the long-term mean SPD*

This section presents the observational limitations of spaceborne radars in terms of missing shallow storms. As described in Section 2.4, SPD is derived from the difference in the detection of per-angle shallow storms with an STH of $\leq$ 2.5 km and the corresponding precipitation rate conditioned on the STH and precipitation type. In this study, a local reference dataset, based on the near-nadir observation, is constructed at a 0.5°-grid resolution. Figure 9a indicates that the shallow-precipitation fraction is a key determinant of the effect of the SPD corrections. For a large part of the high precipitation areas in the tropics, the fraction of precipitation contributed by shallow storms is only a few percentages. This fraction is high in low-rainfall areas over oceans, at high latitudes, over the Tibetan Plateau, and in some mountainous areas (Figs. 9a, b). The correction effect in Fig. 9c is more significant over oceanic low-rainfall areas and at slightly higher latitudes than the LPP correction (Fig. 7a). The impact is less than 1 % in most tropical areas with high precipitation and reached 62 % and 98 % over subtropical oceans where shallow storms contribute 50 % and 80 % of total precipitation, respectively. Over these subtropical oceans, shallow isolated convective-type storms are missing. Precipitation is barely detected at the swath edges over the oceans off the coasts of Peru, Chile, Angola, and Namibia, where the shallow-precipitation fraction is approximately 100 %. At high latitudes, the missing shallow storms consist of both stratiform and convective types. In terms of the zonal average, the highest impact appears around Antarctic waters. These spatial features are similar in all datasets, including TRMM PR Versions 7 and 8 (not shown).

#### *b. Correction based on a lookup table*

The abovementioned SPD calculation requires

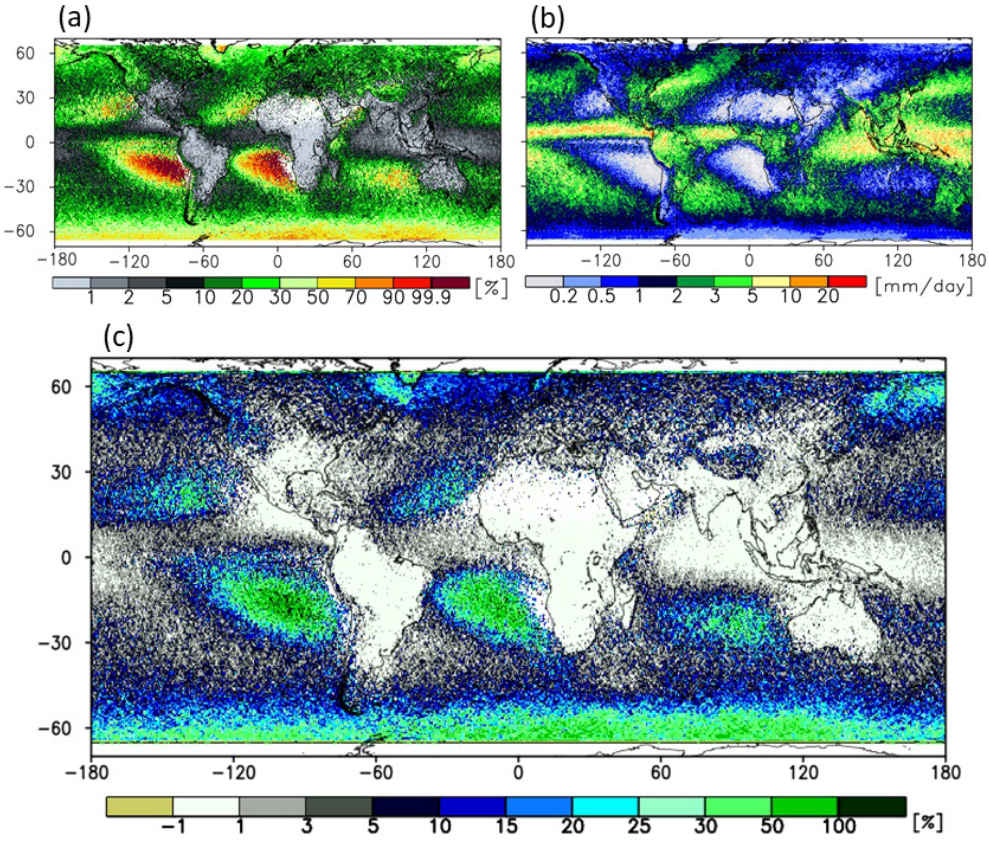


Fig. 9. Maps of the (a) the shallow-precipitation fractions, (b) total precipitation, and (c) effect of the SPD corrections at each 0.5° grid cell. The shallow-precipitation fraction is the proportion of precipitation from storms with top heights of ≤ 2.5 km with respect to the total precipitation.

sufficient samples at moderate spatiotemporal scales. The distribution of the SPD effect corresponds to the fraction of shallow storms and CFB levels. Therefore, the effect is retrieved based on these two parameters using a lookup table (LUT) of the SPD effect (Fig. 10). Higher CFB levels and shallow-precipitation fractions result in a larger SPD correction. For example, for areas with the CFB level 2 km, more than 20 % of precipitation is missing where the shallow-precipitation fraction is > 20 %, whereas more than 50 % of precipitation is missing where the shallow-precipitation fraction is > 40 %. Figure 10 shows that a positive effect is expected even at near-nadir angles where the averaged CFB levels are low because the CFB levels are uneven at the same angle. For instance, LUT shows that a 10 % increase in precipitation is required over areas where the CFB level is approximately 700 m, and shallow-precipitation accounts for half of the total precipitation.

The LUT-based retrieval can be performed wherever the shallow-precipitation fraction is obtained. The SPD correction needs to be extended in short-term and high-resolution statistics to account for seasonal and regional differences in the precipitation structure at middle-to-high latitudes. The availability of near-nadir

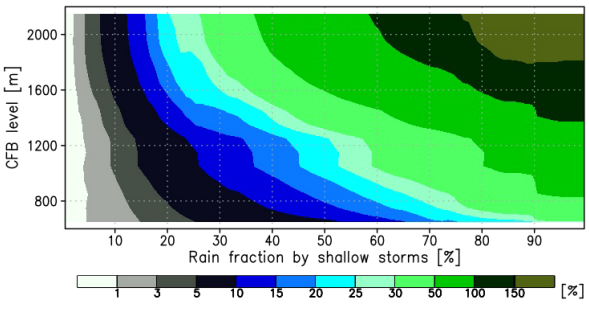


Fig. 10. Lookup table for the SPD effect given the shallow-precipitation fraction and the CFB level.

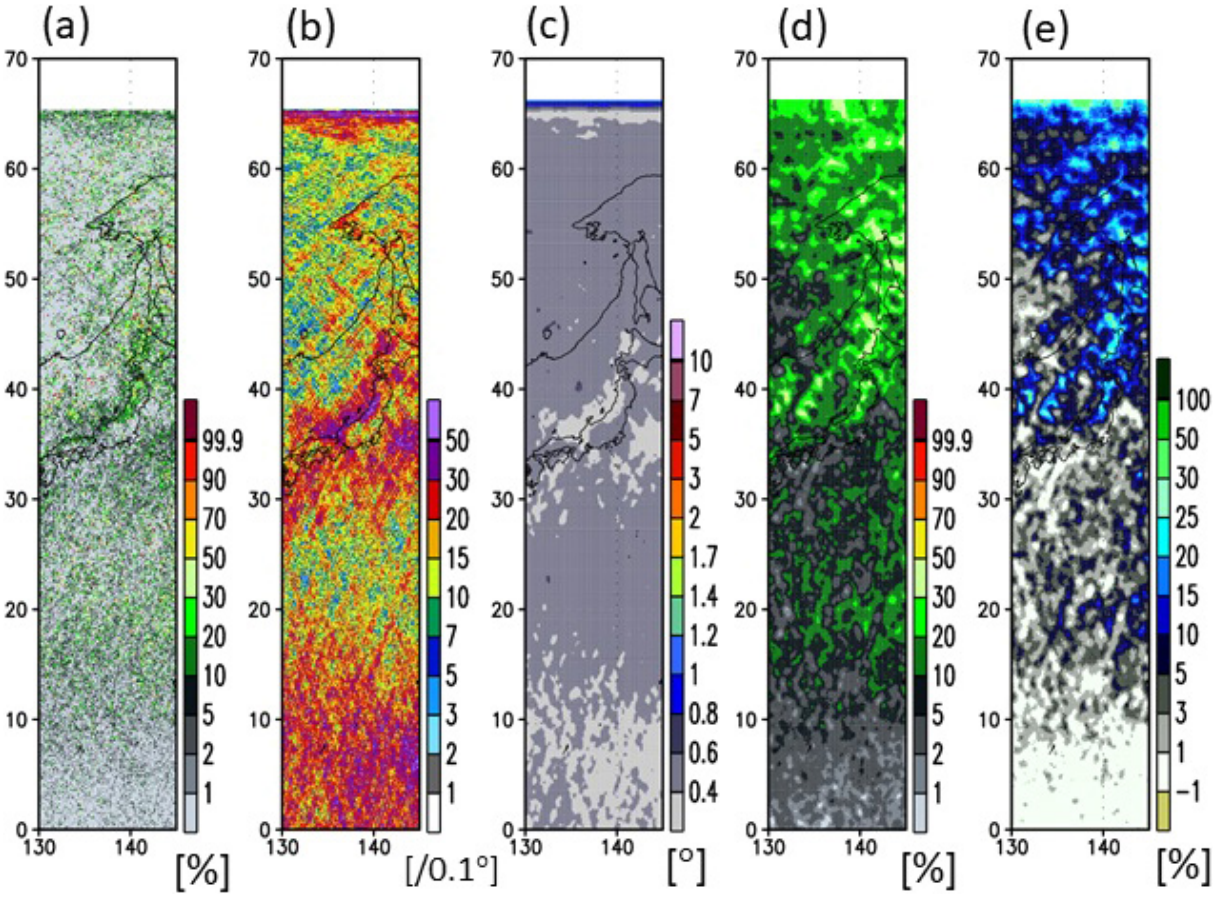


Fig. 11. (a) Fine-scale shallow precipitation fraction mapping by near-nadir data (1998–2013); (b) the number of precipitation samples; (c) the sampling radius ensuring 1,000 precipitation samples; (d) the estimated shallow-precipitation fraction using the neighboring samples within a given radius; and (e) the effect of the LUT-based SPD correction prepared at a resolution of 0.1° for the region 0–70°N and 130–145°E.

shallow-precipitation fraction data at fine spatiotemporal scales is key to short-term SPD corrections. Figure 11a shows the fraction at a scale of 0.1° for the entire period. Grids with extremely high shallow-precipitation fractions occur sporadically, even in the five-year accumulated data, because the number of precipitation samples at each grid is insufficient, as shown in Fig. 11b. Moreover, the spatial distribution of the shallow-precipitation fraction is influenced by a small sample of significant precipitation events. An interpolation scheme has been developed to extract the fine-scale features and ensure sufficient sampling. Herein, we calculate the shallow-precipitation fractions based on 1,000 neighboring precipitation samples for a given period to enhance the sampling ability in order to detect local climatic signals, including high-impact precipitation systems, such as large-scale systems > 100 km with more than 400 precipitation samples. Figure 11c shows the area-equivalent radius of an adjacent area, containing 1,000 precipitation samples for the entire period. Most of the sampling radii are less than 0.6°, except those near the northern and southern edges of the swath and in low-rainfall areas. The radius is shortened according to the data accumulation. The estimated shallow precipitation fraction covers the entire area, including the grids at the edge of the orbit (Fig. 11d). Thus, the SPD effect is retrieved using LUT with the 0.1°-scale CFB levels and the estimated shallow-precipitation fraction data (see Fig. 11e).

The input data need to be spatially averaged to mitigate sampling issues, especially for a short-term dataset. For three months, the fine-scale shallow-precipitation fraction could not be obtained because

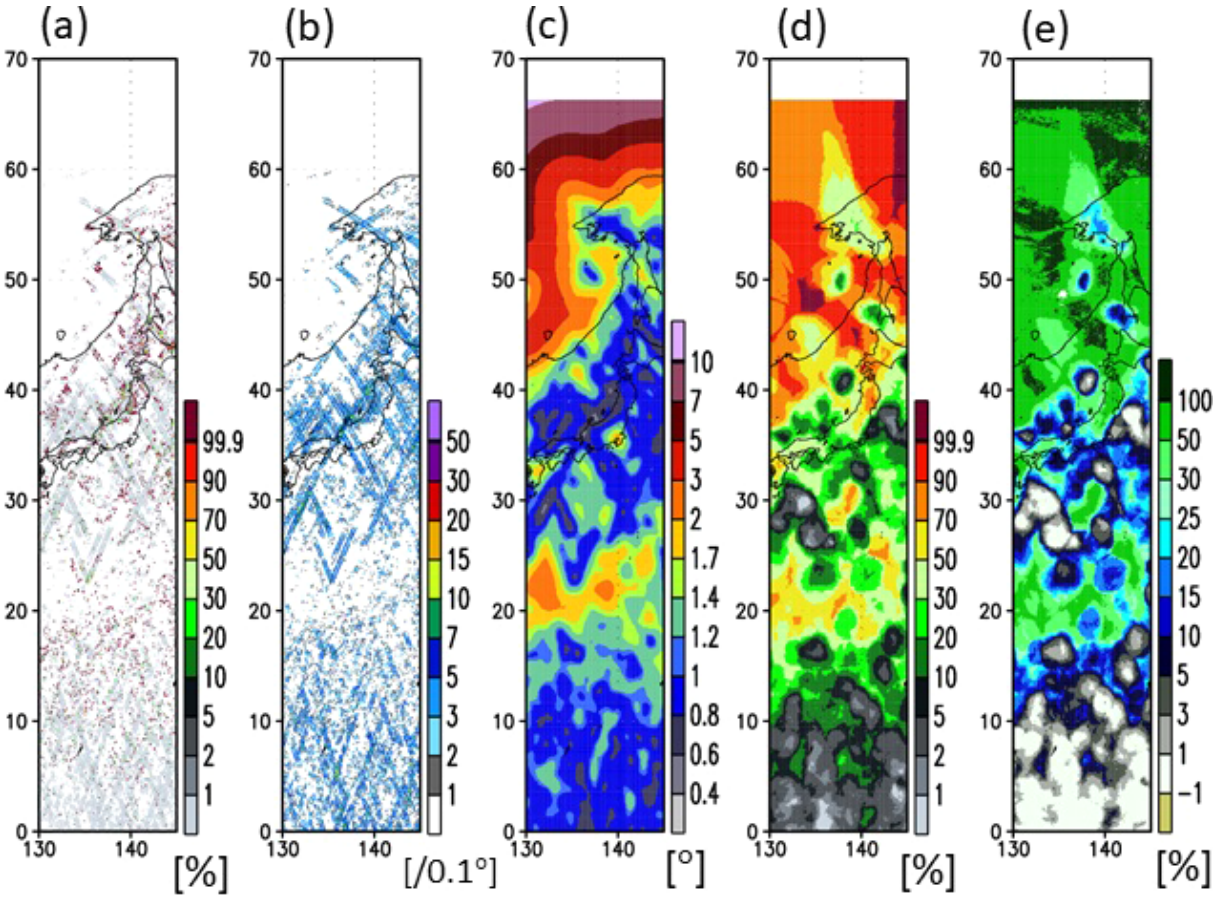


Fig. 12. As contained in Fig. 11 but using data of three months from December 2014 to February 2015.

the near-nadir precipitation samples on a 0.1° grid were scarce and fragmented over most regions (Figs. 12a, b). In other words, sampling gaps need to be filled to perform LUT-based correction. In the three-month data, the area-equivalent radius of the 1,000 precipitation samples ranged from 0.1° to 10°, which are mostly within 2° (Fig. 12c). The sampling radius is approximately 1° over a wide area with moderate and abundant precipitation. Figures 12d and 12e show the estimated shallow-precipitation fraction and the SPD effect, respectively. The shallow-precipitation fraction in Fig. 12d is spatially coherent compared to that in Fig. 12a. The estimated SPD effect for winter precipitation in the northern part of Japan is found to be greater than 50 % (Fig. 12e).

When the sampling radius is set to zero, that is, without the spatial average of the regional shallow-precipitation fraction at a scale of 0.1°, the spatial continuity of the SPD effects is very low, even over the ocean for five-year accumulated data. This study generated 0.1°-grid maps of the shallow-precipitation fractions averaged for each set of 1,000 adjacent precipitation samples. Considering the spatially averaged fraction data and the instantaneous CFB-level information, the SPD effect for every three months could be retrieved from the LUT. This is because the retrieved SPD effect in Fig. 11e matches the analytically derived SPD effect in Fig. 9a. In addition, the LUT-based SPD estimates derived the bias over the mountainous areas where the CFB levels are high, even at nadir. This procedure increases the near-nadir precipitation over the ocean where shallow storms prevail. This implies that a slight increase in the CFB levels could deteriorate the statistics by tens of percentages over low-rainfall oceans, as expected from Fig. 10.

### *3.3 Bias resulting from the main-lobe clutter mask*

#### *a. Total correction amount*

This subsection describes the total bias based on

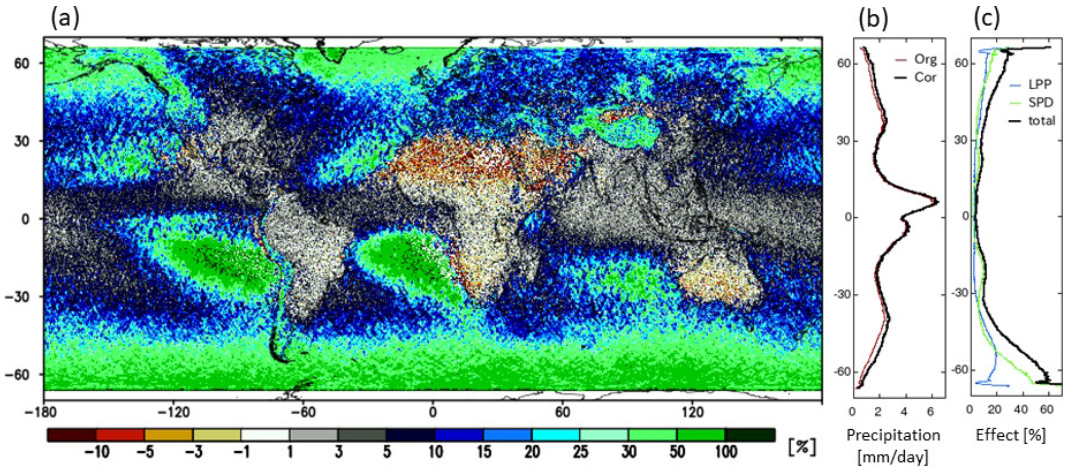


Fig. 13. (a) Map of the combined corrections, (b) zonally averaged precipitation before (Org) and after (Cor) the corrections, and (c) impact of the LPP and SPD corrections on the zonally averaged corrected precipitation. The units are percentages in panels (a) and (c) and mm $d^{-1}$ in panel (b).

Table 2. Mean precipitation and effects of the LPP and SPD corrections over areas between lower latitudes (LOW: 35°S–35°N), higher latitudes (HIGH: 66.3–35°S and 35–66.3°N), and the entire area (ALL: 66.3°S–66.3°N).

| | | Ocean | | | Land | | | All | | |
|---|---|---|---|---|---|---|---|---|---|---|
| | | LOW | HIGH | ALL | LOW | HIGH | ALL | LOW | HIGH | ALL |
| Precipitation [mm $d^{-1}$] | Original | 2.97 | 1.97 | 2.62 | 2.05 | 0.94 | 1.55 | 2.75 | 1.60 | 2.29 |
| | Corrected | 3.19 | 2.39 | 2.92 | 2.12 | 1.12 | 1.67 | 2.93 | 1.94 | 2.54 |
| Correction [%] | LPP | 3.0 | 11.3 | 5.1 | 2.7 | 7.6 | 4.0 | 2.9 | 10.5 | 5.0 |
| | SPD | 4.4 | 10.5 | 6.0 | 0.8 | 11.5 | 3.7 | 3.7 | 10.7 | 5.7 |
| | Total | 7.4 | 21.8 | 11.1 | 3.5 | 19.1 | 7.7 | 6.6 | 21.2 | 10.6 |

the LPP and SPD corrections. Note that there are two types of SPD correction: the gridded analytical solution according to Eq. (1) and the SPD effect referring to LUTs with a per-angle CFB level and estimated shallow-precipitation fractions based on spatially integrated precipitation samples. The latter fine-scale LUT-based estimate is hereinafter the SPD correction.

The total bias map is shown in Fig. 13a. The eventual accumulation effect increases precipitation by less than 10 % in tropical rainy regions and considerably increases precipitation at high latitudes and elevations. On average, these two types of corrections increase the area-weighted mean precipitation by approximately 7, 21, and 11 % over 35°S–35°N, 66.3–35°S and 35–66.3°N, and 66.3°S–66.3°N, respectively (see Table 2). An increase in the zonal precipitation is discerned at middle and high latitudes (Fig. 13b), with impact reaching 56 % in the region with 65–60°S, where shallow storms prevail (Fig. 13c). The averaged correction coefficient is 119 % at latitudes of 66.3–66°S, at the edge of the orbit. The LPP and SPD correction effects are comparable over wide areas, except in subtropical oceans with low precipitation and at high latitudes. At 20°S, the impact on the zonally averaged precipitation is 11 %, whereas the average of the gridded correction coefficient is 26 % (not shown). At high latitudes where the largest effects of the SPD corrections prevail, the LPP correction effectiveness decreases because of lack of observations at levels lower than 1 km. For 65–60°S, thin shallow storms with top heights lower than 2 km provide 90 % of the surface precipitation (not shown). The near-surface precipitation maxima from low-level raindrop growth at high latitudes are difficult to detect.

The revised incidence-angle difference is shown in Fig. 14 and Table 3. The side-lobe effects remain; however, the LPP correction compensates for the bulk of the incidence-angle differences, i.e., the difference

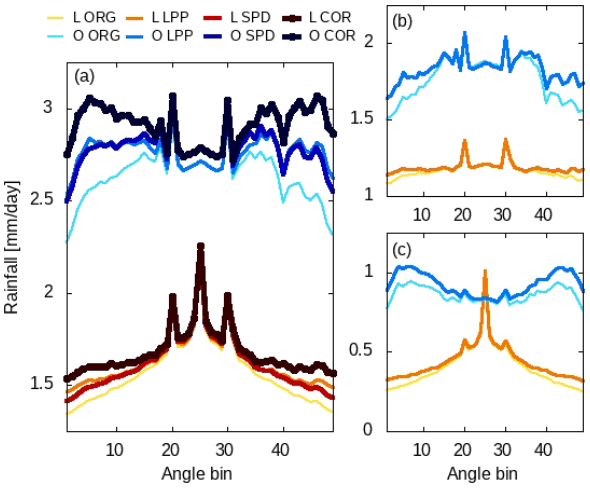


Fig. 14. The per-angle surface precipitation over areas between 66.3°S and 66.3°N for the land (L: warm colors) and ocean (O: cool colors). LPP and SPD in the legend indicate the results from the LPP and the SPD correction, respectively. ORG is the results of original data with no correction. COR indicates the results from data with the LPP and SPD corrections. The plots are based on (a) all the precipitation rates at the surface, (b) the light precipitation rate, $< 10$ mm h$^{-1}$, and (c) the intense precipitation rate, $\geq 10$ mm h$^{-1}$. Panels (b) and (c) show the results of ORG and the LPP correction alone.

between the all-angle precipitation amount and reference near-nadir data, for moderate precipitation rates $< 10$ mm h$^{-1}$ (Figs. 14a, b). The per angle inconsistency in the moderate precipitation, i.e., underestimation concerning the near-nadir statistics, is mitigated by approximately 80 % and 91 % over the land and ocean, respectively. However, positive anomalies occur for intense precipitation ($\geq 10$ mm h$^{-1}$) at off-nadir angles over the ocean. The remarkable incidence-angle difference in the intense precipitation remains over land. The correction mitigates the off-nadir underestimation bias over the land from −8.8 % to −4.1 %, which is a 53 % reduction in the incidence-angle differences. The revised incidence-angle dependency is −4 % and 6 % over the land and ocean, respectively. Therefore, the mitigation in the off-nadir underestimation sheds light on the issue of off-nadir estimations of intense precipitation, i.e., overestimation over the ocean and underestimation over the land. This is not directly associated with the levels of the main-lobe clutter interference but with the attenuation correction per angle over land and ocean. Approximately half of the remaining bias over land can decrease when the off-nadir intense precipitation is equivalent to the near-nadir statistics. It is worthy to note that the LPP-corrected surface precipitation data at angle bins 20 and 30 are 20 % and 16 % greater than the data in the other bins for moderate and all precipitation, respectively, over the land but 7 % and 13 % larger, respectively, over the ocean. The mitigation of the side-lobe contamination reduced the averaged surface precipitation by 0.5–1 % over the ocean. In addition, the LPP-corrected data indicate that the extraordinary peak at a nadir over the land is 2.4 times larger than the data in the other bins, and it is 1.9 times larger than the near-nadir data for intense precipitation (Fig. 14c). This remains to be determined in further discussions of extreme events based on a single-frequency radar.

Regarding the precipitation with low attenuation, given by the final estimate of PIA $< 1$ dB, fractions in the sample, precipitation amount, and LPP correction effect account for 92, 52, and 66 %, respectively (not shown). The fraction in the LPP correction effect rises to 89 % for profiles with PIA $< 6$ dB. Considering the low usage of SRT for light precipitation in the KuPR 06A algorithm (Seto et al. 2021), the impact of PIA inconsistency, due to the LPP correction, is limited in total precipitation amount. The retrieval of heavy precipitation demands the continual refinement of schemes on attenuation estimates, as well as other issues, such as the non-uniform beam-filling effect.

Table 3. Precipitation anomaly in the near-nadir statistics over areas between 66.3°S and 66.3°N. The unit is %. LT10 and GE10 indicate the statistics from instantaneous surface precipitation rates lower than 10 mm h$^{-1}$ and greater than or equal to 10 mm h$^{-1}$, respectively.

| | Original | | | LPP | | | SPD | Total |
|---|---|---|---|---|---|---|---|---|
| | All | LT10 | GE10 | All | LT10 | GE10 | All | All |
| Land | −8.8 | −2.1 | −23.9 | −6.2 | −0.4 | −19.1 | −6.8 | −4.1 |
| Ocean | −1.6 | −4.5 | 4.9 | 3.2 | −0.4 | 11.1 | 0.6 | 5.6 |

Table 4. Summary of the global precipitation data used in this study.

| Acronym | Full name | Version | Reference |
|---|---|---|---|
| CPC_Global | Climate Prediction Center unified gauge-based analysis of precipitation | V1.0 | Xie et al. (2007) |
| GPCC_MP | Global Precipitation Climatology Centre Monitoring product | V6 | Schneider et al. (2018) |
| CMORPH_CRT | Bias-corrected CPC MORPHing technique | V1.0ADJ | Xie et al. (2017) |
| GSMaP_Gauge | Gauge-adjusted Global Satellite Mapping of Precipitation (GSMaP) | V7 | Mega et al. (2019) |
| PERSIANN_CDR | Precipitation Estimation from Remotely Sensed Information using Artificial Neutral Networks–Climate Data Record | V1R1 | Ashouri et al. (2015) |
| GPCP_CDR | Global Precipitation Climatology Project Climate Data Record | V1.3 | Adler et al. (2017b) |
| IMERG_Cal | IMERG with gauge calibration | V6 | Huffman et al. (2019) |
| GSMaP_MWR | GSMaP based on MicroWave Radiometers | V7 | Aonashi et al. (2009) |
| GSMaP_MVK | GSMaP based on a Moving Vector with Kalman filter | V7 | Ushio et al. (2009) |
| IMERG_HQ | IMERG microwave-only precipitation estimates | V6 | Huffman et al. (2019) |
| IMERG_Uncal | IMERG without gauge calibration | V6 | Huffman et al. (2019) |

*b. Comparison of global precipitation products*

In this section, we compare the abovementioned corrected KuPR precipitation data with other high-resolution multisatellite and gauge-based precipitation datasets. The 11 products used for the comparison provide latest observational data between 60°S and 60°N from June 2014 to May 2019 (Table 4). The datasets are grouped into three types: gauge-based products, including CPC_Globe and GPCC_MP; satellite-gauge blended datasets, including CMORPH_CRT, GSMaP_Gauge, PERSIANN_CDR, GPCP_CDR, and IMERG_Cal; and satellite-only precipitation estimates, including GSMaP_MWR, GSMaP_MVK, IMERG_HQ, and IMERG_Uncal. These state-of-the-art precipitation datasets are used by various scientific communities, and various studies are ongoing regarding their error performance and algorithm development (e.g., Wang and Yong 2020; Yuan et al. 2019; Beck et al. 2020; Kubota et al. 2020b). Precipitation data at different spatial resolutions are averaged over the range of 1°-scale grid, while ocean and land grid pixels are identified on the basis of 5-min gridded global-relief data (ETOPO5), according to the dominant surface types for each 1° scale grid. The areal-weighted averages over the land and ocean at latitudes between 60°S and 60°N are summarized in Fig. 15. The KuPR precipitation without and with the correction are 2.41 mm $d^{-1}$ and 2.65 mm $d^{-1}$, respectively. The satellite-gauge blended and satellite-only products estimated precipitation of 2.91 mm $d^{-1}$ and 3.09 mm $d^{-1}$, respectively. The difference in KuPR with respect to the satellite-gauge blended products improves from −17 % to −9 %, whereas that with satellite-only products improves from −22 % to −14 %. Thus, a large reduction in the differences at high latitudes exists.

Furthermore, the mean precipitation of the gauge-based, satellite-gauge blended, and satellite-only products are 2.10, 2.26, and 2.58 mm $d^{-1}$, respectively. The land precipitation of the satellite-only products over land is 23 % greater than the gauge-based analysis. The satellite-gauge blended precipitation data reduce this inconsistency, but they are still 8 % greater than the gauge-based data. The CPC_Global precipitation is 15 % less than GPCC_MP precipitation. The satellite-gauge blended products adjusted using the CPC unified daily gauge analysis (CMORPH_CRT and GSMaP_Gauge) have 13 % less precipitation than those adjusted using the GPCC data (PERSIANN_CDR, GPCP_CDR, and IMERG_Cal). In contrast, the original KuPR precipitation (KuPR_ORG) and corrected KuPR precipitation (KuPR_COR) are 19 % and 15 % less than the gauge-based mean precipitation, respectively. The differences between KuPR_ORG and CPC_Globe, and KuPR_COR and CPC_Globe are −12 % and −7 %, respectively. Therefore, the difference between the corrected KuPR precipitation and gauge-based analysis is near 10 %, whereas the KuPR precipitation remains smaller than the near-nadir statistics and other satellite datasets, as indicated in Figs. 14 and 15. For areas between 50°S and 50°N, the KuPR_COR precipitation increases by 5 % compared to those between 60°S and 60°N (not shown). The non-negligible differences from the correction and different latitudinal zones underscore the need to

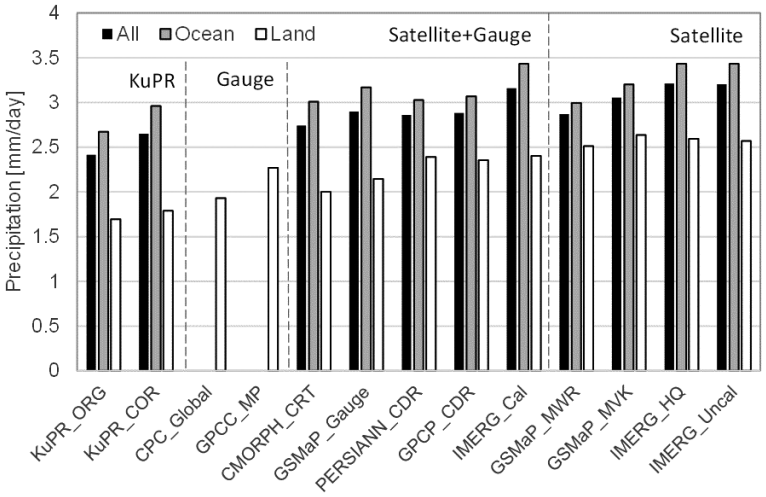


Fig. 15. Mean precipitation using KuPR without (KuPR_ORG) and with (KuPR_COR) corrections and the gauge-based observational data (CPC_Global and GPCC_MP), the satellite-gauge-blended precipitation datasets (CMORPH_CRT, GSMaP_Gauge, PERSIANN_CDR, GPCP_CDR, and IMERG_Cal), and the satellite-only precipitation products (GSMaP_MWR, GSMaP_MVK, IMERG_HQ, and IMERG_Uncal) for the period of June 2014–May 2019. The data are gridded at a resolution of 1° and averaged over land and ocean between 60°S and 60°N.

obtain robust precipitation estimates at high latitudes.

The KuPR_ORG, KuPR_COR, and other satellite-based mean precipitation rates over ocean are 2.67, 2.96, and 3.20 mm $d^{-1}$, respectively. The KuPR precipitation increases by 11 % because of the correction. The KuPR_ORG and KuPR_COR precipitation over the ocean are 16 % and 7 % less than those of other satellite-related products, respectively. The refined KuPR precipitation is nearly equivalent to several oceanic precipitation estimates and the conventional precipitation climatology (Behrangi et al. 2014); however, there remain uncertainties to be addressed, e.g., detecting limits of light precipitation at high latitudes. Attention should be paid to the remaining incidence-angle dependency of the KuPR_COR precipitation over the ocean, especially for intense precipitation, as shown in Fig. 14.

## 4. Conclusions

GPM DPR detects precipitation profiles over land and ocean, and over complex terrain, from 66.3°S to 66.3°N. This study investigated regional retrieval uncertainties in near-surface precipitation statistics caused by main-lobe clutter removal routines and incidence-angle differences. The GPM DPR KuPR precipitation data are 7 % and 2 %, respectively, lower than the reference near-nadir data over land and ocean. The underestimation bias increased to 9 % at latitudes higher than 35°. This study investigated the low-level profiles and missing shallow storms to mitigate such internal inconsistencies. Our results show that the LPP and SPD corrections increase the land-surface precipitation by 8 % and reduce the angle-bin difference by half for the total precipitation over land and 80 % for moderate precipitation of < 10 mm $h^{-1}$. This mitigates the off-nadir underestimation of the surface precipitation statistics from the different CFB levels to some extent and reduces the retrieval differences between the precipitation datasets. The inconsistency between the KuPR precipitation and gauge-based analysis decreased by half. Precipitation increased because of corrections by 11 % and 21 % at latitudes between 66.3°S and 66.3°N and above 35°, respectively. Table 2 summarizes results from the retrieval process and the observational limits, with respect to low-level precipitation. The refined KuPR precipitation is 9 % lower than that of the satellite-gauge blended products. The uncertainties retrieved by the LPP and SPD corrections are large at high latitudes, where shallow storms consist of the bulk of the total precipitation, because the profiling capability near the surface and sensitivity with light snowfall detection are insufficient. Therefore, these retrieval uncertainties are present in the current product. The assumption with the constant $Z_e$ below the CFB level in the DPR algorithm (Seto et al. 2021) needs to be improved. The LPP-

corrected surface precipitation data are incorporated as a variable named precipRateESurface2 in a new version (Version 07) of the GPM DPR product released in 2021.

Therefore, the corrections indicate that the off-nadir overestimation of intense precipitation retrieval over the ocean needs to be resolved because of its blur by the off-nadir underestimation of light and moderate precipitation. This reaffirms the importance of careful investigations of attenuation corrections in single-frequency analyses (Meneghini et al. 2015, 2021). The incidence-angle dependence of intense precipitation over land remains one of the most important challenges to achieving robust estimations and understanding extreme precipitation biases (Masunaga et al. 2019). Other remaining issues are related to the LPP correction of the vertical variation in precipitation adjacent to the surface, i.e., at altitudes of < 1 km, which require comprehensive validation studies into phase transitions and hydrometeors. Note that a detailed examination of the impact of specific profiles archived in the current LPP database is beyond the scope of this study. However, an accumulation of various samples will increase our understanding of the specifying factors of the precipitation-rate profiles. Additionally, the differences in the near-nadir data produced by different sensors need to be examined. Our preliminary study demonstrates that the TRMM PR Version 8 product data based on the DPR Version 06A algorithm differ considerably from the TRMM PR Version 7 data, regarding the incidence-angle pattern of the surface precipitation. Efforts to mitigate biases resulting from the algorithms will fill these gaps in the data.

Approximately 60 % of corrections that reduce the underestimation of the original data are attributed to the observational limits of SPD, although the fractions vary by region. This study suggests SPD corrections for short-term data using LUTs and the spatial averaging of shallow-precipitation fraction data. For instantaneous estimates, the use of additional information, such as brightness temperatures or assimilation techniques, is necessary. The effect of the missing shallow storms is conspicuous over complex terrain and at high latitudes, where uncertainties in observations are large. Finer-resolution and higher-sensitivity sensors, capable of detecting the caps of storms, are needed to evaluate global and local water budgets.

## Acknowledgments

The authors express gratitude to members of the TRMM and GPM projects. We are grateful to the reviewers for their constructive comments, which improved the manuscript. This study was supported by the JAXA eighth GPM/TRMM research announcements, the JAXA second research announcement on the Earth Observations, and JSPS KAKENHI Grant Number 19H01969.

## References

Adler, R. F., G. Gu, M. Sapiano, J.-J. Wang, and G. J. Huffman, 2017a: Global precipitation: Means, variations and trends during the satellite era (1974–2014). *Surv. Geophys.*, **38**, 679–699.

Adler, R. J.-J. Wang, M. Sapiano, G. Huffman, D. Bolvin, E. Nelkin, and NOAA CDR Program, 2017b: *Global Precipitation Climatology Project (GPCP) Climate Data Record (CDR), version 1.3 (daily)*. NOAA National Centers for Environmental Information, doi: 10.7289/V5RX998Z.

Aoki, S., and S. Shige, 2021: Large precipitation gradients along the south coast of Alaska revealed by spaceborne radars. *J. Meteor. Soc. Japan*, **99**, 5–25.

Aonashi, K., J. Awaka, M. Hirose, T. Kozu, T. Kubota, G. Liu, S. Shige, S., Kida, S. Seto, N.Takahashi, and Y. N. Takayabu, 2009: GSMaP passive, microwave precipitation retrieval algorithm: Algorithm description and validation. *J. Meteor. Soc. Japan*, **87A**, 119–136.

Ashouri, H., K.-L. Hsu, S. Sorooshian, D. K. Braithwaite, K. R. Knapp, L. D. Cecil, B. R. Nelson, and O. P. Prat, 2015: PERSIANN-CDR: Daily precipitation climate data record from multi-satellite observations for hydrological and climate studies. *Bull. Amer. Meteor. Soc.*, **96**, 69–83.

Awaka, J., M. Le, V. Chandrasekar, N. Yoshida, T. Higashiuwatoko, T. Kubota, and T. Iguchi, 2016: Rain type classification algorithm module for GPM Dual-Frequency Precipitation Radar. *J. Atmos. Oceanic Technol.*, **33**, 1887–1898.

Barros, A. P., and M. Arulraj, 2020: Remote sensing of orographic precipitation. *Satellite Precipitation Measurement.* Levizzani, V., C. Kidd, D. Kirschbaum, C. Kummerow, K. Nakamura, and F. Turk (eds.), *Advances in Global Change Research*, **69**, Springer, 559–582.

Beck, H. E., E. F. Wood, M. Pan, C. K. Fisher, D. G. Miralles, A. I. J. M. van Dijk, T. R. McVicar, and R. F. Adler, 2019: MSWEP V2 global 3-hourly 0.1° precipitation: Methodology and quantitative assessment. *Bull. Amer. Meteor. Soc.*, **100**, 473–500.

Beck, H. E., N. Vergopolan, M. Pan, V. Levizzani, A. I. J. M. van Dijk, G. P. Weedon, L. Brocca, F. Pappenberger, G. J. Huffman, and E. F. Wood, 2020: Global-scale evaluation of 22 precipitation datasets using gauge observations and hydrological modeling. *Satellite Precipitation Measurement*. Levizzani, V., C. Kidd, D. Kirschbaum, C. Kummerow, K. Nakamura, and F. Turk. (eds.), *Advances in Global Change Research*,

**69**, Springer, 625–653.

Behrangi, A., G. Stephens, R. F. Adler, G. J. Huffman, B. Lambrigtsen, and M. Lebsock, 2014: An update on the oceanic precipitation rate and its zonal distribution in light of advanced observations from space. *J. Climate*, **27**, 3957–3965.

Casella, D., G. Panegrossi, P. Sanò, A. C. Marra, S. Dietrich, B. T. Johnson, and M. S. Kulie, 2017: Evaluation of the GPM-DPR snowfall detection capability: Comparison with CloudSat-CPR. *Atmos. Res.*, **197**, 64–75.

Hamada, A., and Y. N. Takayabu, 2016: Improvements in detection of light precipitation with the Global Precipitation Measurement dual-frequency precipitation radar (GPM/DPR). *J. Atmos. Oceanic Technol.*, **33**, 653–667.

Hamada, A., Y. N. Takayabu, C. Liu, and E. J. Zipser, 2015: Weak linkage between the heaviest rainfall and tallest storms. *Nat. Commun.*, **6**, 6213, doi:10.1038/ncomms7213.

Heymsfield, A. J., C. Schmitt, C.-C.-J. Chen, A. Bansemer, A. Gettelman, P. R. Field, and C. Liu, 2020: Contributions of the liquid and ice phases to global surface precipitation: Observations and global climate modeling. *J. Atmos. Sci.*, **77**, 2629–2648.

Hirose, M., 2011: *Incidence angle dependency check. Evaluation of TRMM PR 2A25 v.7 (ITE233)*. JAXA Web site, detailed validation results by Japanese PR Validation Team, 8 pp. [Available at https://www.eorc.jaxa.jp/TRMM/documents/PR_algorithm_product_information/doc_pr_v7/A10_v7val_hirose110608.pdf.]

Hirose, M., and K. Nakamura, 2004: Spatiotemporal variation of the vertical gradient of rainfall rate observed by the TRMM Precipitation Radar. *J. Climate*, **17**, 3378–3397.

Hirose, M., S. Shimizu, R. Oki, T. Iguchi, D. A. Short, and K. Nakamura, 2012: Incidence-angle dependency of TRMM PR rain estimates. *J. Atmos. Oceanic Technol.*, **29**, 192–206.

Hirose, M., Y. N. Takayabu, A. Hamada, S. Shige, and M. K. Yamamoto, 2017: Spatial contrast of geographically induced rainfall observed by TRMM PR. *J. Climate*, **30**, 4165–4184.

Hou, A. Y., R. K. Kakar, S. Neeck, A. A. Azarbarzin, C. D. Kummerow, M. Kojima, R. Oki, K. Nakamura, and T. Iguchi, 2014: The Global Precipitation Measurement mission. *Bull. Amer. Meteor. Soc.*, **95**, 701–722.

Huffman, G. J., D. T. Bolvin, D. Braithwaite, K. Hsu, R. Joyce, C. Kidd, E. J. Nelkin, S. Sorooshian, J. Tan, and P. Xie, 2019: NASA Global Precipitation Measurement (GPM) Integrated Multi-satellitE Retrievals for GPM (IMERG). *Algorithm Theoretical Basis Document (ATBD) version 06*, 38 pp. [Available at https://gpm.nasa.gov/sites/default/files/document_files/IMERG_ATBD_V06.pdf.]

Iguchi, T., 2020: Dual-Frequency Precipitation Radar (DPR) on the Global Precipitation Measurement (GPM) mission's Core Observatory. *Satellite Precipitation Measurement*. Levizzani, V., C. Kidd, D. Kirschbaum, C. Kummerow, K. Nakamura, and F. Turk (eds.), *Advances in Global Change Research*, **67**, Springer, 183–192.

Iguchi, T., T. Kozu, J. Kwiatkowski, R. Meneghini, J. Awaka, and K. Okamoto, 2009: Uncertainties in the rain profiling algorithm for the TRMM Precipitation Radar. *J. Meteor. Soc. Japan*, **87A**, 1–30.

Iguchi, T., S. Seto, R. Meneghini, N. Yoshida, J. Awaka, M. Le, V. Chandrasekar, S. Brodzik, and T. Kubota, 2018: *GPM/DPR Level-2 Algorithm Theoretical Basis Document*. 127 pp. [Available at https://www.eorc.jaxa.jp/GPM/doc/algorithm/ATBD_DPR_201811_with_Appendix3b.pdf.]

Kirstetter, P.-E., Y. Hong, J. J. Gourley, M. Schwaller, W. Petersen, and J. Zhang, 2013: Comparison of TRMM 2A25 products, version 6 and version 7, with NOAA/NSSL ground radar-based national mosaic QPE. *J. Hydrometeor.*, **14**, 661–669.

Kobayashi, K., S. Shige, and M. K. Yamamoto, 2018: Vertical gradient of stratiform radar reflectivity below the bright band from the Tropics to the extratropical latitudes seen by GPM. *Quart. J. Roy. Meteor. Soc.*, **144**, 165–175.

Kojima, M., T. Miura, K. Furukawa, Y. Hyakusoku, T. Ishikiri, H. Kai, T. Iguchi, H. Hanado, and K. Nakagawa, 2012: Dual-frequency precipitation radar (DPR) development on the global precipitation measurement (GPM) core observatory. *Proceeding SPIE 8528, Earth Observing Missions and Sensors: Development, Implementation, and Characterization II*, **85281A**, doi:10.1117/12.976823.

Kozu, T., T. Kawanishi, H. Kuroiwa, M. Kojima, K. Oikawa, H. Kumagai, K. Okamoto, M. Okumura, H. Nakatsuka, and K. Nishikawa, 2001: Development of precipitation radar onboard the Tropical Rainfall Measuring Mission (TRMM) satellite. *IEEE Trans. Geosci. Remote Sens.*, **39**, 102–116.

Kubota, T., N. Yoshida, S. Urita, T, Iguchi, S. Seto, R. Meneghini, J. Awaka, H. Hanado, S. Kida, and R. Oki, 2014: Evaluation of precipitation estimates by at-launch codes of GPM/DPR algorithms using synthetic data from TRMM/PR observations. *IEEE J. Sel. Top. Appl. Earth Obs. Remote Sens.*, **7**, 3931–3944.

Kubota, T., T. Iguchi, M. Kojima, L. Liao, T. Masaki, H. Hanado, R. Meneghini, and R. Oki, 2016: A statistical method for reducing sidelobe clutter for the Ku-band precipitation radar on board the GPM Core Observatory. *J. Atmos. Oceanic Technol.*, **33**, 1413–1428.

Kubota, T., S. Seto, M. Satoh, T. Nasuno, T. Iguchi, T. Masaki, J. M. Kwiatkowski, and R. Oki, 2020a: Cloud assumption of precipitation retrieval algorithms for the Dual-Frequency Precipitation Radar. *J. Atmos. Oceanic Technol.*, **37**, 2015–2031.

Kubota, T., K. Aonashi, T. Ushio, S. Shige, Y. N. Takayabu, M. Kachi, Y. Arai, T. Tashima, T. Masaki, N. Kawamoto, T. Mega, M. K. Yamamoto, A. Hamada, M. Yamaji, G. Liu, and R. Oki, 2020b: Global Satellite Mapping of Precipitation (GSMaP) products in the GPM era. *Satellite Precipitation Measurement. vol. 1*. Levizzani, V., C. Kidd, D. Kirschbaum, C. Kummerow, K. Nakamura, and F. Turk (eds.), *Advances in Global Change Research*, **67**, Springer, 355–373.

Kummerow, C., W. Barnes, T. Kozu, J. Shiue, and J. Simpson, 1998: The Tropical Rainfall Measuring Mission (TRMM) sensor package. *J. Atmos. Oceanic Technol.*, **15**, 809–817.

Liu, C., and E. J. Zipser, 2013: Why does radar reflectivity tend to increase downward toward the ocean surface, but decrease downward toward the land surface? *J. Geophys. Res.: Atmos.*, **118**, 135–148.

Liu, C., and E. J. Zipser, 2015: The global distribution of largest, deepest and most intense precipitation systems. *Geophys. Res. Lett.*, **42**, 3591–3595.

Masaki, T., T. Iguchi, K. Kanemaru, K. Furukawa, N. Yoshida, T. Kubota, and R. Oki, 2020: Calibration of the dual-frequency precipitation radar onboard the Global Precipitation Measurement Core observatory. *IEEE Trans. Geosci. Remote Sens.*, 1–16.

Masunaga, H., M. Schröder, F. A. Furuzawa, C. Kummerow, E. Rustemeier, and U. Schneider, 2019: Inter-product biases in global precipitation extremes. *Environ. Res. Lett.*, **14**, 125016, doi:10.1088/1748-9326/ab5da9.

Mega, T., T. Ushio, T. Matsuda, T. Kubota, M. Kachi, and R. Oki, 2019: Gauge-adjusted global satellite mapping of precipitation. *IEEE Trans. Geosci. Remote Sens.*, **57**, 1928–1935.

Meneghini, R., J. A. Jones, T. Iguchi, K. Okamoto, and J. Kwiatkowski, 2004: A hybrid surface reference technique and its application to the TRMM precipitation radar. *J. Atmos. Oceanic Technol.*, **21**, 1645–1658.

Meneghini, R., H. Kim, L. Liao, J. A. Jones, and J. M. Kwiatkowski, 2015: An initial assessment of the surface reference technique applied to data from the dual-frequency precipitation radar (DPR) on the GPM satellite. *J. Atmos. Oceanic Technol.*, **32**, 2281–2296.

Meneghini, R., H. Kim, L. Liao, J. Kwiatkowski, and T. Iguchi, 2021: Path attenuation estimates for the GPM Dual-frequency Precipitation Radar (DPR). *J. Meteor. Soc. Japan*, **99**, 181–200.

Nakamura, K., 2021: Progress from TRMM to GPM. *J. Meteor. Soc. Japan*, **99**, 697–729.

Oki, R., T. Iguchi, and K. Nakamura, 2020: The GPM DPR validation program. *Satellite Precipitation Measurement. vol. 2*. Levizzani, V., C. Kidd, D. Kirschbaum, C. Kummerow, K. Nakamura, and F. Turk (eds.), *Advances in Global Change Research*, **69**, Springer, 503–514.

Porcacchia, L., P.-E. Kirstetter, V. Maggioni, and S. Tanelli, 2019: Investigating the GPM Dual-frequency Precipitation Radar signatures of low-level precipitation enhancement. *Quart. J. Roy. Meteor. Soc.*, **145**, 3161–3174.

Schneider, U., A. Becker, P. Finger, A. Meyer-Christoffer, and M. Ziese, 2018: *GPCC Monitoring Product: Near Real-Time Monthly Land-Surface Precipitation from Rain-Gauges based on SYNOP and CLIMAT data*. Global Precipitation Climatology Centre at Deutscher Wetterdienst, Germany, doi:10.5676/DWD_GPCC/MP_M_V6_100.

Seto, S., and T. Iguchi, 2007: Rainfall-induced changes in actual surface backscattering cross sections and effects on rain-rate estimates by spaceborne precipitation radar. *J. Atmos. Oceanic Technol.*, **24**, 1693–1709.

Seto, S., T. Iguchi, and T. Oki, 2013: The basic performance of a precipitation retrieval algorithm for the global precipitation measurement mission's single/dual-frequency radar measurements. *IEEE Trans. Geosci. Remote Sens.*, **51**, 5239–5251.

Seto, S., T. Iguchi, R. Meneghini, J. Awaka, T. Kubota, T. Masaki, and N. Takahashi, 2021: The precipitation rate retrieval algorithms for the GPM Dual-frequency Precipitation Radar. *J. Meteor. Soc. Japan*, **99**, 205–237.

Skofronick-Jackson, G., W. A. Petersen, W. Berg, C. Kidd, E. F. Stocker, D. B. Kirschbaum, R. Kakar, S. A. Braun, G. J. Huffman, T. Iguchi, P. E. Kirstetter, C. Kummerow, R. Meneghini, R. Oki, W. S. Olson, Y. N. Takayabu, K. Furukawa, and T. Wilheit, 2017: The Global Precipitation Measurement (GPM) Mission for Science and Society. *Bull. Amer. Meteor. Soc.*, **98**, 1679–1695.

Sohn, H.-J., and B.-J. Sohn, 2015: Two heavy rainfall types over the Korean peninsula in the humid East Asian summer environment: A satellite observation study. *Mon. Wea. Rev.*, **143**, 363–382.

Stephens, G. L., J. Li, M. Wild, C. A. Clayson, N. Loeb, S. Kato, T. L'Ecuyer, P. W. Stackhouse Jr., M. Lebsock, and T. Andrews, 2012: An update on Earth's energy balance in light of the latest global observations. *Nat. Geosci.*, **5**, 691–696.

Sun, Q., C. Miao, Q. Duan, H. Ashouri, S. Sorooshian, and K.-L. Hsu, 2018: A review of global precipitation data sets: Data sources, estimation, and intercomparisons. *Rev. Geophys.*, **56**, 79–107.

Terao, T., F. Murata, Y. Yamane, M. Kiguchi, A. Fukushima, M. Tanoue, S. Ahmed, S. A. Choudhury, H. J. Syiemlieh, L. Cajee, A. K. Bhagabati, P. Bhattacharya, S. Dutta, R. Mahanta, and T. Hayashi, 2017: Direct validation of TRMM/PR near surface rain over the Northeastern Indian subcontinent using a tipping bucket raingauge network. *SOLA*, **13**, 157–162.

TRMM Precipitation Radar Team, 2011: *Tropical Rainfall Measuring Mission (TRMM) Precipitation Radar algorithm*. Instruction manual for version 7, 175 pp. [Available at https://www.eorc.jaxa.jp/TRMM/docu

ments/PR_algorithm_product_information/pr_manual/PR_Instruction_Manual_V7_L1.pdf.]

Ushio, T., K. Sasashige, T. Kubota, S. Shige, K. Okamoto, K. Aonashi, T. Inoue, N., Takahashi, T. Iguchi, M. Kachi, R. Oki, T. Morimoto, and Z. Kawasaki, 2009: A Kalman filter approach to the Global Satellite Mapping of Precipitation (GSMaP) from combined passive microwave and infrared radiometric data. *J. Meteor. Soc. Japan*, **87A**, 137–151.

Wang, H., and B. Yong, 2020: Quasi-global evaluation of IMERG and GSMaP precipitation products over land using gauge observations. *Water*, **12**, 243, doi:10.3390/w12010243.

Xie, P., M. Chen, S. Yang, A. Yatagai, T. Hayasaka, Y. Fukushima, and C. Liu, 2007: A gauge-based analysis of daily precipitation over East Asia. *J. Hydrometeor.*, **8**, 607–626.

Xie, P., R. Joyce, S. Wu, S.-H. Yoo, Y. Yarosh, F. Sun, and R. Lin, 2017: Reprocessed, bias-corrected CMORPH global high-resolution precipitation estimates from 1998. *J. Hydrometeor.*, **18**, 1617–1641.

Yuan, F., L. Zhang, K. M. W. Soe, L. Ren, C. Zhao, Y. Zhu, S. Jiang, and Y. Liu, 2019: Applications of TRMM- and GPM-era multiple-satellite precipitation products for flood simulations at sub-daily scales in a sparsely gauged watershed in Myanmar. *Remote Sens.*, **11**, 140, doi:10.3390/rs11020140.